

Hydraulic fracture growth and migration of induced microseismicity: Application of a fully coupled hydromechanical FDEM approach

Murad S. Abuaisha, David Eaton, Jeffrey Priest, Ron Wong

▶ **To cite this version:**

Murad S. Abuaisha, David Eaton, Jeffrey Priest, Ron Wong. Hydraulic fracture growth and migration of induced microseismicity: Application of a fully coupled hydromechanical FDEM approach. Microseismic Industry Consortium: Annual Research Report, Volume 7, 2016. hal-02461116

HAL Id: hal-02461116

https://minesparis-psl.hal.science/hal-02461116

Submitted on 3 Feb 2020

HAL is a multi-disciplinary open access archive for the deposit and dissemination of scientific research documents, whether they are published or not. The documents may come from teaching and research institutions in France or abroad, or from public or private research centers.

L'archive ouverte pluridisciplinaire **HAL**, est destinée au dépôt et à la diffusion de documents scientifiques de niveau recherche, publiés ou non, émanant des établissements d'enseignement et de recherche français ou étrangers, des laboratoires publics ou privés.

Chapter 5

Hydraulic fracture growth and migration of induced microseismicity: Application of a fully coupled hydromechanical FDEM approach

Murad AbuAisha[a,b]*, David Eaton*[a]*, Jeffrey Priest*[b] *and Ron Wong*[b]

[a] *Dept. of Geoscience, Univ. of Calgary, Calgary, AB, T2N 1N4, Canada. E: morad_77_2@hotmail.com*

[b] *Dept. of Civil Engineering, Univ. of Calgary, Calgary, AB, T2N 1N4, Canada.*

5.1 Abstract

This work provides a fully coupled hydromechanical FDEM approach to report on the relation of hydraulic fracture growth and spatio–temporal distribution of induced microseismicity. A case study of a Hydraulic Fracturing (HF) test implemented at the Evie formation of the Horn River basin, Canada, was used for verification of the numerical simulations. In a first step, the field injection profile has been simulated until shutdown, when the numerical fracture radius was correlated to the radial distribution of field induced seismicity. Another published literature that provides diffusional envelopes to describe migration of induced microseismicity correlates well to our findings. In a second step, we investigated the role of fully coupled hydromechanics on generating microseismic events due to mechanical slip of stressed pre–existing joints. It was observed that though the fracture radius and its growth direction give good indication about microseismicity, fully coupled hydromechanics is necessary to account for fracture–offset microseismic events, as well as other events at the onset of breakdown; i.e. due to dissipation of fracturing energy in the rock formation.

5.2 Introduction

Hydraulic Fracturing (HF) is a technique for enhancing the permeability of a rockmass by injecting high–pressure fluids in order to initiate/open fractures in the rocks (*AbuAisha et al.*, 2016; *AbuAisha and Loret*, 2016a;b). The technique is widely used by the oil and gas industry in the development of low permeability shale reservoirs (*AbuAisha et al.*, 2016). The growth of a tensile fracture system is accompanied by stress changes, fluid leakoff and pore pressure diffusion into the formation (*Economides and Nolte*, 2003). During HF, brittle fracturing of the intact rock, or reactivation of pre–existing critically stressed fractures, releases energy that can be observed as microseismic events (*Rutledge et al.*, 1998). Monitoring

of induced microseismic events is commonly used to estimate hydraulic fracture growth, discrete fracture network activation, and stimulated reservoir volume (*House*, 1987; *Eaton*, 2014). A number of techniques that are rooted in microseismic observations have been developed to aid in the interpretation of fracturing processes. It is often assumed that the time-dependent microseismic cloud is a proxy for the growth of the hydraulic fracture. Based on this assumption, *Boroumand and Eaton* (2015) developed a geomechanical simulation in which model parameters for an energy-based fracture simulation are tuned to fit observed microseismicity in space and time. Shapiro and co–workers (*Shapiro and Dinske*, 2009a;b; *Shapiro et al.*, 2006) have developed a poroelastic approach based on the concept of a seismicity-triggering front. This approach assumes a diffusion model that is characterized by either constant diffusivity, where the triggering front has a parabolic form, or pressure-dependent diffusivity, in which case a cubic–parabolic triggering front emerges under certain assumptions. In general, the simplified models underlying these approaches do not capture the complexity of the actual spatial distribution of microseismic events (*Cornet*, 2000).

In this paper we use a fully coupled hydro–mechanical Finite–Discrete Element Modelling (FDEM) approach to investigate the link between microseismicity and hydraulic fracture propagation in more detail. The FDEM approach, implemented using the Irazu code (*Lisjak et al.*, 2017), enables history matching of the field injected pressure profile until shutdown. The model is also able to consider the simulated HF induced microseismicity, either due to opening of hydraulic fractures or shear–slip of randomly distributed pre–existing joints. The post fracturing fluid pressure behaviour is analysed, and the fracture envelope (simulated fracture length versus time) is correlated to the field spatio–temporal microseismic cloud. The objective of this work is to gain insights into how the evolving numerical fractures correlate to the microseismic cloud. We apply this approach to analyze a microseismic dataset recorded during a hydraulic fracture treatment in the Horn River basin of northeast British Columbia, Canada.

5.3 Hydraulic fracturing by FDEM

The FDEM approach was first suggested by *Munjiza et al.* (1995). It is a hybrid technique that combines the advantages of the FEM and DEM approaches. While the medium is undergoing elastic deformation, the behaviour of intact material is explicitly modelled by FEM. As the strength of the material is exceeded, fractures are initiated, giving rise to discontinuous blocks where the interaction between these blocks is captured by DEM. The FDEM approach is capable of tracking fracture initiation and propagation by applying the principles of nonlinear elastic fracture mechanics (*Barenblatt*, 1962). In this study we use an implementation of the FDEM method (the Irazu code) that discretizes the modelling domain with a mesh of elastic triangular Delaunay elements connected to each other by non–dimensional rectangular cohesive fracture elements at their edges (Fig. 1). An explicit time integration scheme is employed to solve the equation of motion of the discretized system during numerical simulations. The Irazu code has been discussed and verified against analytical solutions (*Lisjak et al.*, 2017).

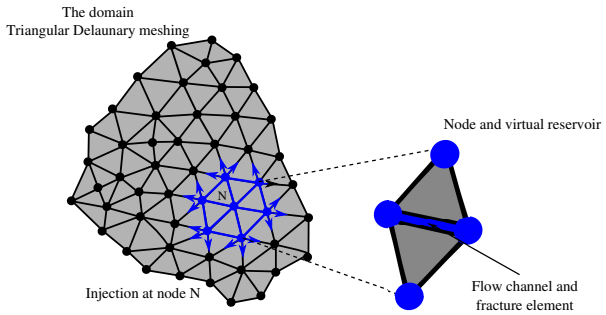


Figure 1 Conceptual graph that illustrates the Delaunay triangulation and the implementation of fluid diffusion in the Irazu code. The flow takes place in flow channels that are initially assigned a finite aperture corresponding to the formation permeability. Each virtual reservoir, where fluid pressure is calculated, receives a mass of fluid from all branching channels.

Hydraulic fracturing in our simulations is implemented by considering the existence of flow channels that coincide with the fracture elements in the initial mesh (Fig. 1) (*Lisjak et al.*, 2017). The nodes of the triangular elements represent virtual reservoirs where fluid pressure and fluid mass are sequentially calculated. The apertures of the flow channels are assigned initial values to mimic the initial permeability of the porous medium. Fluid is injected at node N, and due to pressure gradients, it propagates to adjoining nodes (virtual reservoirs) through the flow channels. If the fluid injection rate is greater than the dissipation of fluid pressure through the flow channels, the fluid pressure will eventually lead to breaking of the fracture elements and a fracture initiates. The code can also account for true/physical fluid cavities like boreholes for instance, see *Lisjak et al.* (2017) for more details.

5.4 Numerical modelling: simulations and discussion

A field hydraulic fracturing test performed within the Horn River Basin (Evie formation) is used as a reference for development of the numerical model and subsequent simulations. In a first step, the section initially defines the model setup and the material properties pertaining to the rock formation. The numerical simulations start by matching the field injection pressure profile, the numerical bi–wing fracture radius (fracture envelope) is then correlated to the radial distribution of the field induced microseismicity. For quantitative comparison, the cubic–parabolic analytical triggering front of *Shapiro and Dinske* (2009b) is plotted against our numerical fracture envelope and field seismicity. The role of fully coupled hydromechanics on generating microseismicity, i.e. by mechanical slip of critically stressed joints, is investigated, where the spatio–temporal distribution of numerical induced microseismicity explains the field behaviour. The section ends by discussing the failure nature of two events that are typical for our model: event A represented by a far critically stressed joint tip that fails due to mechanical deformation created by fracture growth (mode II failure); and event B on the fracture trajectory that fails due to fluid pressure (opening/mode I).

5.4.1 Model setup and material properties

The field test is representative of a long horizontal well penetrating into the Evie formation of thickness 400 m. A 2–D vertical domain containing the two major far–field stresses is modelled as shown in Fig. 2. To capture the onset of fracturing and map the evolution of fractures, the element mesh is intensively refined with 0.8 m elements in a 200 m $\times$ 200 m zone centred at the injection point. Element size is gradually increased to 5.0 m from this zone to the boundary edge. Fluid injection in the borehole is modelled as a point source at a node of an element within the center of the domain, since only large scale fracturing and induced microseismicity are of interest rather than the near–borehole behaviour. The figure also shows the permeable nature of the far–field boundaries.

Table 1 shows the material and fluid properties pertaining to the porous medium. The *in situ* stress measurements correspond to a Total Vertical Depth TVD of 2890 m. The 2–D far–field stresses are $\sigma_V = 70$ MPa and $\sigma_H = 75$ MPa. The initial reservoir pressure is 33.9 MPa and the rock permeability is in the order of $k \sim (O^{-19})$ m^2 (*Chou et al.*, 2011). Since the medium can be assumed impermeable for the time–frame of our simulations (2.6 hours), and consequently flow is restricted to fractures, Biot's coefficient (κ) is set equal to 1. Numerical fluid injection history follows that applied in the field, i.e. increasing linearly to 0.16 l/s at breakdown, then kept constant until shutdown.

A set of randomly distributed joints with average length of 1.60 m and fracture density of 0.1/m^2 was created in the zone of intensive refinement (Fig. 2b). These joints can only sustain shear strength based on Mohr–Coulomb criterion (Eq. 5.1) expressed in terms of the residual/fracture friction angle (ϕ_f) and the normal effective stresses ($\sigma_n^{'}$) (*Lisjak et al.*, 2017),

$$f_r = -\sigma_n^{'} \tan(\phi_f), \tag{5.1}$$

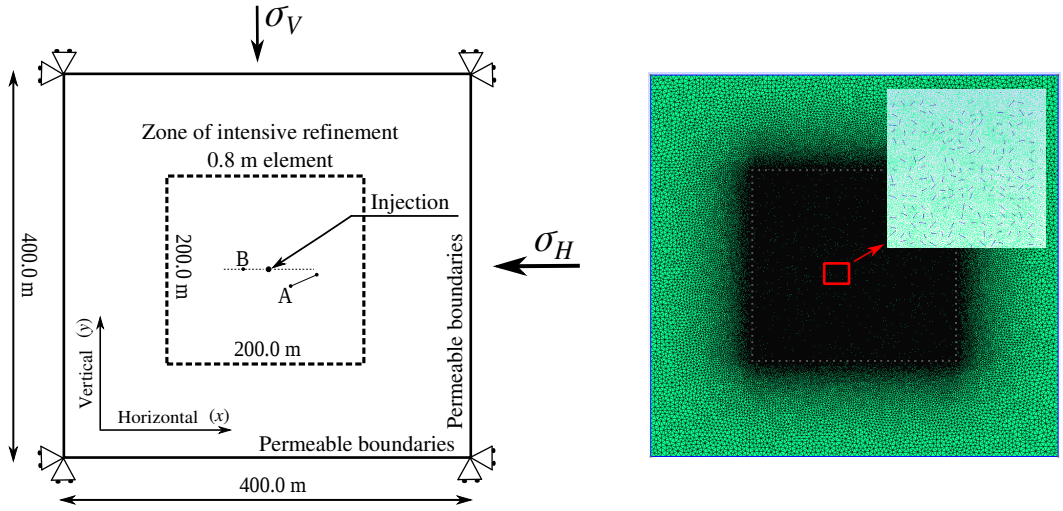
f_r the frictional resistance. Fluid flow inside the joints is controlled by the permeability assigned to the rock formation and by Darcy's law. The joints are introduced in the model to explore possible microseismic events due to shear–slip incited by mechanical rock deformation. The fracturing process is expected to perturb the stress field, which will instigate critically stressed joints to slip based on Eq. 5.1 (*AbuAisha et al.*, 2016; *Bruel*, 2007). We limit the extent of these joints to the 200 m $\times$ 200 m zone for computational ease. Two random points; a joint–tip point A, and point B on the expected hydraulic fracture trajectory, are displayed to investigate the failure mechanisms (modes II and I) associated with our model.

5.4.2 Numerical simulations and discussion

Figure (3) shows the simulated injection pressure (dotted line) correlated to the field injection history (solid). There is a relatively good fit between the two responses; the numerical elastic behaviour, before breakdown, is reasonably representative of the field one, the breakdown pressure is accurately matched, and the post–peak breakdown response until shutdown is fairly well correlated.

Our simulations generated a bi–wing hydraulic fracture growing in the direction of the maximum far–field stress σ_H. The numerical radius growth of the hydraulic fracture is calculated at each time step (fracture envelope). Figure 4 shows the spatio–temporal radial migration of the field microseismicity (black dots) plotted against the numerical fracture envelope (red line). The location of each microseismic event is calculated with respect to the injection well.

Shapiro and co–workers (*Shapiro and Dinske*, 2009a;b; *Shapiro et al.*, 2006) suggested that the evolution of a hydraulic fracture can be treated as an end–member of a diffusional triggering front. Their approach assumes that such a front propagates like the process of pore pressure relaxation in isotropic poroelastic saturated medium. For



(a) (b)

Figure 2 (a) The geometry and boundary conditions of domain chosen for the HF simulations and induced seismicity. (b) Triangular Delaunay meshing of the domain showing refinement of element size approaching the wellbore: A zoom–in is displayed to show the random distribution of pre–existing joints. Points A and B are displayed to investigate the loading paths during the fracturing process.

Table 1 Fluid and material properties pertaining to the porous medium (*Chou et al.*, 2011).

Nature	Parameter	Value	Unit
Elasticity	Drained Young's modulus, E	24.5	GPa
	Drained Poisson's ratio, ν	0.2	-
Fracture	Tensile strength, f_t	5.2	MPa
	Cohesion, c	13.5	MPa
	Mode I fracture energy, G_{Ic}	10	N/m
	Mode II fracture energy, G_{IIc}	100	N/m
	Material internal friction angle, ϕ_i	35	(°)
	Fracture friction angle, ϕ_f	35	(°)
Fluid flow	Dynamic viscosity, μ	0.5×10^{-3}	Pa.s
	Permeability, k	(O^{-19})	m^2
	Biot's coefficient, κ	1.0	-
	Compressibility, K_f	2.2×10^9	MPa

this, they assumed either a linear fluid diffusion (parabolic front) based on Biot's system with constant diffusivity, or a nonlinear diffusion (cubic–parabolic front) characterized by the equation of fluid mass balance and Darcy's law with possible significant permeability/diffusivity increase. In this work, we are using the cubic–parabolic diffusional front (Eq. 5.2) suggested by *Shapiro and Dinske* (2009b),

$$r = A\left(\frac{Q_I\, t}{\Phi}\right)^{1/3}, \tag{5.2}$$

where r is the radial growth of the triggering front, Q_I is the injection flow rate, A is a dimensionless geometric factor, and Φ is the additional porosity created by fractures. If we assume a value of $A = (3/4\pi)^{1/3}$ for spherical fractured domain, and Φ to be linearly proportional to the fracture size, we will get $\Phi = 1.133 \times 10^{-4}\%$ for a fracture radius of 68 m (Fig. 4), compared to $\Phi = 0.001\%$ for ~600 m fracture as suggested by *Shapiro and Dinske* (2009b) for Barnett shale. For an injection rate of $Q_I = 0.16$ l/s, the cubic prabolic diffusional front of Shapiro can be plotted against the field induced microseismicity (Fig. 4 blue dashed line). It can be seen that the fracture envelope obtained during our simulations and that given by the model of Shapiro approximates the migration

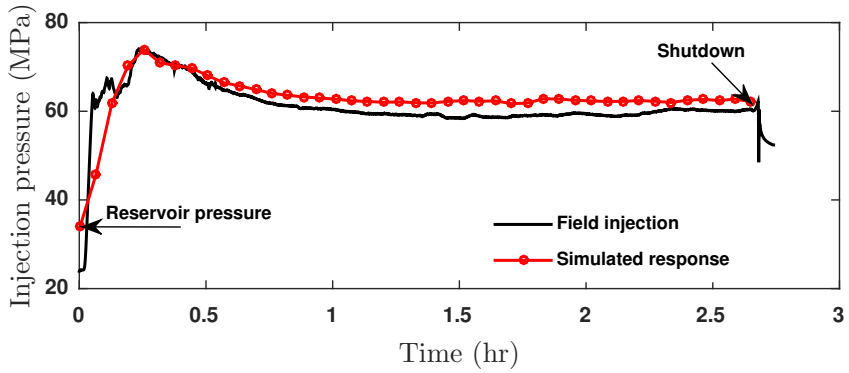


Figure 3 Irazu numerical injection response correlated to the field injection history until shutdown (∼2.6 hours).

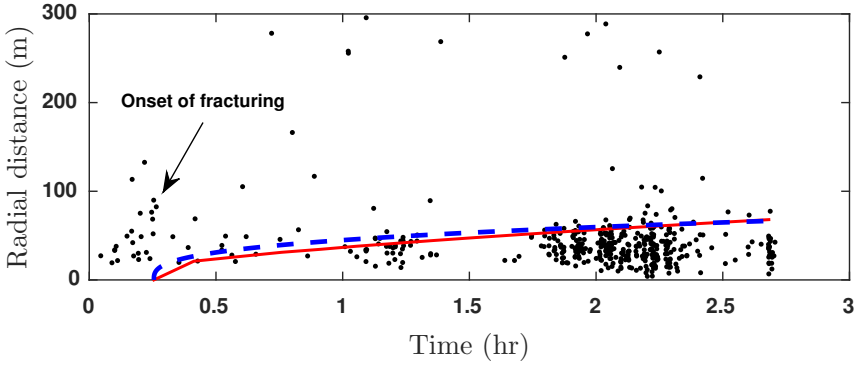


Figure 4 Spatio–temporal migration of the field microseismicity. Figure also shows the fracture envelope derived from our simulations (red solid) and Shapiro's nonlinear diffusional envelope (*Shapiro and Dinske*, 2009b) shown by the blue dashed line.

of the microseismic cloud obtained during the field fracture test. Suggesting that the use of microseismic data can give a reasonably good indication of the geometry of hydraulic fractures and their growth direction. However, it can be seen that numerous isolated microseismic events are located outside of the fracture envelope.

To consider the possible cause of these isolated events, Fig. 5 shows the radial distribution of simulated microseismic events generated by shear–slip of the randomly distributed joints (Fig. 2b). The presented microseismic events are obtained at discrete time steps during the simulation. In addition, low magnitude microseismic events caused by the hydraulic fracture tensile opening are omitted.

Similar to the field microseismicity (Fig. 4), the simulated HF gives rise to a considerable number of microseismic events at the onset of fracturing that correspond to the time recorded for the breakdown pressure (Fig. 3). However, in the field response, these initial microseismic events are more dispersed and are thought to relate to the sequence of breakdown pressures that are observed prior to the peak breakdown pressure. The microseismic events recorded at the onset of fracturing are seen to occur up to ∼125 m away from the injection point in both the field and the simulations, and are not related to the tensile fracturing of the rock. These events are initiated due to critically stressed joints being perturbed by the release of stored elastic energy propagating in the rock mass due to the initial opening of the bi-wing fracture. As the fracture propagates in the rock, the microseismic cloud follows the fracture envelope, however, some events still occur offset from this main fracture. Since the rock medium is impermeable for the time–frame of our simulations, these fracture–offset events are also attributed to the mechanical deformation; i.e. close–by critically stressed joints shear–slip due to perturbations in the displacement/stress field as the hydraulic fracture grows/opens.

Figure 6a shows the $p - q$ loading paths for two points; a joint–tip point A at radial distance 29.5 m and reflex orientation of 218.82° (Figs 2a and 5), and a random point on the bi–wing fracture trajectory (Fig. 2a). The quantities p and q are defined as the mean of the effective principal stress tensor ($p = (\sigma_1^{'} + \sigma_2^{'})/2$), and the magnitude of the deviatoric effective principal stress tensor

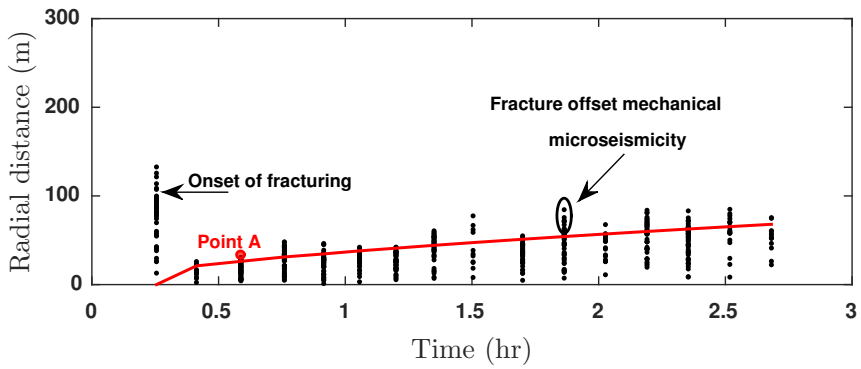


Figure 5 Radial distribution of simulated microseismic events with time. Figure also shows the calculated numerical fracture envelope highlighted in Fig. 4.

($q = |\sigma_1^{'} - \sigma_2^{'}|/2$). The failure envelope (Eq. 5.1) can be expressed in terms of p and q as shown in Fig. 6a.

The two loading paths start from the same point/initial effective stress state. As soon as fluid reaches point B on the fracture trajectory, effective stresses become tensile and the loading path grows to touch the tensile failure envelope ($q = f_t$, blue dotted line), which is characterized by mode I failure. However, for point A, and since it is located on a joint tip/weak zone, the dissipation of energy at breakdown reduces (in algebraic sense) the initial effective stress state and gets the joint close to failure, which is represented by the first linear change of the dry loading path (black part). The path then continues to grow (red part) until it touches the failure envelope, which is characterized by mode II failure and shear–slip microseismic event. The path then yields to the failure envelope before it starts to show unloading behaviour. However, this reduction in initial stresses depends on the orientation of joints, as some orientations, and depending on the anisotropy of the far–field stresses, are more favourable to slippery.

The total injection volume for this test was estimated to 1450 l in 2.65 hr, and the numerical maximum vertical opening at the injection point of the hydraulic fracture was ∼8.5 mm. The displacement magnitude history at point A has shown a sudden increase at breakdown, then it continued to grow slightly before it started to increase considerably at the onset of shear–slip (Fig. 6b).

5.5 Conclusion

A fully coupled hydro–mechanical FDEM approach has been introduced to simulate hydraulic fracture growth and subsequent migration of induced microseismicity. While modelling the HF test at the Evie formation, our simulations showed a bi–wing fracture growing in the direction of the horizontal maximum far–field stress σ_H. In accordance with published literature, the numerical fracture radius has been seen to correlate well to the radial distribution of field microseismicity. Results of previous published work, which provide nonlinear diffusional envelopes to describe microseismic event migration, were utilized to verify our numerical results, where good fit was observed. However, a fully coupled hydromechanics was needed to simulate microseismic events that are incited by mechanical shear–slip of pre–existing joints, both at the onset of fracturing and during fracture growth.

5.6 Acknowledgments

The author would like to thank the sponsors of the Microseismic Industry Consortium for financial support.

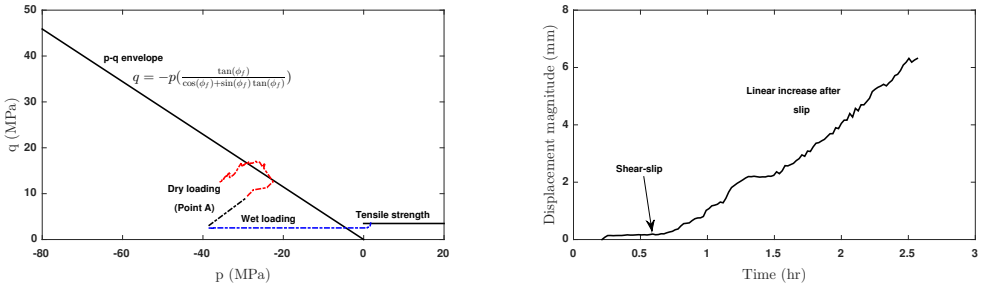
5.7 References

AbuAisha, M., Loret, B., and Eaton, D. (2016). Enhanced Geothermal Systems (EGS): Hydraulic fracturing in a thermo–poroelastic framework. *Journal of Petroleum Science and Engineering* 146, 1179–1191.

AbuAisha, M., and Loret, B. (2016)a. Influence of hydraulic fracturing on impedance and efficiency of thermal recovery from HDR reservoirs. *Geomechanics for Energy and the Environment*, doi:10.1016/j.gete.2016.02.001.

AbuAisha, M., and Loret, B. (2016)b. Stabilization of forced heat convection: Applications to Enhanced Geothermal Systems (EGS). *Transport in Porous Media* 112, 229–252.

AbuAisha, M., Eaton, D., Priest, J., and Wong, R. (2016). Hydro-Mechanically coupled Finite-Discrete Element Modelling (FDEM) approach to simulate hydraulic fracturing in isotropic and fractured rock formations.



(a) Loading paths and $p - q$ envelope

(b) Displacement magnitude at point A

Figure 6 (a) $p - q$ loading paths for two points: point A (Figs 2a and 5) presented by dotted black and red line (shear–slip, mode II failure); and point B (Fig. 2a) on the fracture trajectory presented by dotted blue line (tensile mode I failure). (b) Displacement magnitude history at point A: The figure shows sudden increase at the onset of fracturing followed by a slight growth before it starts to increase significantly at shear–slip.

Journal of Petroleum Science and Engineering, (Undergoing reviews).

Economides, J. M., and Nolte G. K. (2003). Reservoir stimulation. *John Wiley & Sons Ltd*, third edition.

Rutledge, T. J., Scott Phillips, W., and Schuessler, K. B. (1998). Reservoir characterization using oil–production–induced microseismicity, Clinton County, Kentucky. *Tectonophysics* 289, 129–152.

House, L. (1987). Locating microearthquakes induced by hydraulic fracturing in Crystalline rock. *Geophysical Research Letters* 14, 919–921.

Eaton, D. (2014). Alberta Telemetered Seismograph Network (ATSN): Real–time Monitoring of Seismicity in Northern Alberta. *Recorder* 39, No. 09.

Boroumand, N., and Eaton, D.(2015). Energy–based hydraulic fracture numerical simulation: Parameter selection and model validation using microseismicity. *Geophysics*, doi:10.1190/geo2014-0091.1.

Shapiro, A. S., and Dinske, C. (2009)a. Scaling of seismicity induced by nonlinear fluid–rock interaction. *Journal of Geophysical Research* 114, doi:10.1029/2008JB006145.

Shapiro, A. S., and Dinske, C. (2009)b. Fluid-induced seismicity: Pressure diffusion and hydraulic fracturing. *Geophysical Prospecting* 57, 301–310.

Shapiro, A. S., Dinske, C., and Rothert E. (2006). Hydraulic–fracturing controlled dynamics of microseismic clouds. *Geophysical Research Letters* 33, doi:10.1029/2006GL026365.

Cornet, F. (2000). Comment on 'Large-scale in situ permeability tensor of rocks from induced microseismicity' by S. A. Shapiro, P. Audigane and J.-J. Royer. *Geophysical Journal International* 140, 465–469.

Lisjak, A., Kaifosh, P., He, L., Tatone, B. S. A., Mahabadi, O. K., and Grasselli, G. (2017). A 2D, fully–coupled, hydro–mechanical, FDEM formulation for modelling fracturing processes in discontinuous, porous rock masses. *Computers and Geotechnics* 81, 1–18.

Munjiza, A., Owen, D. R. J., and Bicanic, N. A. (1995). A combined finite–discrete element method in transient dynamics of fracturing solids. *Engineering Computations* 12, 145–174.

Barenblatt, G. I. (1962). The mathematical theory of equilibrium cracks in brittle fracture. *Advances in Applied Mechanics* 7, 55–129.

Chou, Q., Gao, J., and Somerwil M. (2011). Analysis of geomechanical data for Horn River Basin gas shales, NE British Columbia, Canada. In the SPE Middle East unconventional gas conference and exhibition, Paper SPE 142498, Muscat, Oman, 31 January – 2 February 2011.

Bruel, D. (2007). Using the migration of the induced seismicity as a constraint for fractured Hot Dry Rock reservoir modelling. *International Journal of Rock Mechanics and Mining Sciences* 44, 1106–1117.